# Modeling MEK inhibitor-Associated Retinopathy *in vitro* using human induced pluripotent stem cell-derived retinal pigment epithelial cells

Lola P. Lozano[1,2], Madeleine Jennisch[1,2], Renato Jensen[1,2], Jason A. Ratcliff[3], Luke A. Wiley[1,2], Brynnon Harman[1,2], Megan J. Riker[1,2], Allison T. Wright[1,2], Bradley A. Erickson[4], H. Culver Boldt[1,2], Timothy M. Boyce[1,2], Robert F. Mullins[1,2], Elaine M. Binkley[1,2], Budd A. Tucker*[1,2]

[1]Institute for Vision Research, The University of Iowa, Iowa City, IA, 52242, USA

[2]Department of Ophthalmology and Visual Sciences, The University of Iowa Carver College of Medicine, Iowa City, IA, 52242, USA

[3]Iowa Institute of Human Genetics, Bioinformatics Division, The University of Iowa, Iowa City, IA, 52242, USA

[4]Department of Urology, The University of Iowa Carver College of Medicine, Iowa City, IA, 52242, USA

*Budd A. Tucker

4111 Medical Education Research Facility, 375 Newton Road, Iowa City, Iowa 52246

+1.319.353.4488

budd-tucker@uiowa.edu

The authors have declared that no conflict of interest exists.

**Abstract**

Pharmacologic inhibitors of MEK are important anti-cancer drugs but can result in MEK inhibitor-Associated Retinopathy (MEKAR) in which vision is lost due to serous retinal detachments that form via an unknown mechanism. We hypothesized that the cause of this side effect is drug-induced dysfunction of retinal pigment epithelial (RPE) cells. To test this hypothesis, we used human induced pluripotent stem cell-derived RPE cells. We treated mature, hiPSC-derived RPE cells with selumetinib and measured impacts on RPE-specific function, structure, and gene expression. Selumetinib increases the ability of hiPSC-derived RPE to internalize bovine rod outer segments (1.9 vs 3.0, p=0.0024). It also decreases expression of aquaporin 1 during the first 10 days of treatment (2.7 vs 1.1, p=0.0015). It has no effect on the ability of hiPSC-derived RPE to maintain membrane integrity. Selumetinib alters gene expression of hiPSC-derived RPE, with significant changes in genes involved in transport of ions and small molecules regulating cell volume and lysosomal acidification. Selumetinib may lead to subretinal fluid accumulation by both increasing secretions into this space and decreasing outflow.

47 **INTRODUCTION**

48 Many cancers develop activating mutations in the cell signaling mitogen-activated
49 protein kinase/extracellular signal-regulated kinase (MAPK/ERK) pathway which lead to
50 uncontrolled cell survival and proliferation (**Supplementary Figure 1A**) (1). Mutations in
51 *MEK* frequently occur in cutaneous melanoma, non-small cell lung cancer, and
52 pancreatic, colorectal, breast, and liver cancers. Four MEK inhibitors have received
53 FDA approval for clinical use: cobimetinib for malignant melanoma with $BRAF^{V600}$
54 mutations, binimetinib and trametinib for metastatic melanoma with $BRAF^{V600E/K}$
55 mutations, and selumetinib for patients with Neurofibromatosis Type 1 and stage III or
56 IV differentiated thyroid cancer. There is also evidence suggesting the efficacy of MEK
57 inhibitors in the treatment of the basal subtype of bladder cancer and metastatic
58 castration resistant prostate cancer (2, 3).

59

60 Unfortunately, due to the ubiquity of the MAPK/ERK pathway, MEK inhibitor therapy has
61 a substantial number of side effects, some of which are quite significant. For instance,
62 one of the more common side effects reported, affecting up to 90% of patients (4), is
63 MEK inhibitor-Associated Retinopathy (MEKAR). On average, MEKAR manifests within
64 the first two weeks of starting MEK inhibitor therapy (5). The retinopathy is typically
65 multifocal and bilateral with findings isolated to the posterior pole along the main
66 vascular arcades and macula. There is often at least one focus localized to the fovea,
67 which causes loss of high acuity, central vision (5). In all cases of documented MEKAR
68 and retinopathies due to other drugs inhibiting the MAPK/ERK pathway, fluid
69 accumulates between the ends of the photoreceptor outer segments at the

70 interdigitation zone with an intact retinal pigment epithelium (RPE) (**Supplementary**
71 **Figure 1B-C**) (5-7). This fluid accumulation is not due to abnormal fluid leakage from
72 the choroidal vasculature, as seen in central serous chorioretinopathy, which is
73 demonstrated by no leakage of dye on fluorescein angiography (4, 5, 8-10). While
74 MEKAR often resolves spontaneously by approximately 32 days after starting
75 treatment, a subset of patients have persistent retinopathy and severe visual side
76 effects requiring their medication be discontinued (5, 10).
77
78 Although the mechanism of MEKAR is unknown, given the robust clinical phenotype
79 (subretinal fluid accumulation without leakage), it is postulated to be the result of drug-
80 induced RPE cell dysfunction. RPE cells, which form a monolayer below the neural
81 retina above the choroidal vasculature, are critical for maintaining retinal homeostasis
82 (**Supplementary Figure 1D-E**). For instance, RPE cells play a key role in
83 phagocytosing shed photoreceptor outer segments (POS), scavenging reactive oxygen
84 species secreting growth factors for both the retina and underlying choroid, and
85 contributing to the choroid-retinal barrier via tight junction proteins (zonula occludens,
86 occludins, claudins) and transporting molecules between these two structures (11-13).
87 Their role in molecular trafficking, maintaining subretinal fluid volume as well as the
88 proper ionic concentrations for photoreceptors to function, exists because of the unique
89 protein polarity on the basolateral versus apical side of the RPE plasma membrane
90 (12). We hypothesize that drug-induced disruption of these unique RPE cell functions
91 causes the pathologic subretinal fluid accumulation observed in patients with MEKAR.
92

93 To investigate, we generated human induced pluripotent stem cell-derived RPE cells
94 and treated them with the clinically used MEK inhibitor, selumetinib. As most patients
95 manifest MEKAR within the first two weeks of beginning MEK inhibitor therapy, and
96 many individuals experience resolution by 1-month, we collected data after treating cells
97 for 10, 20, and 30 days. While we did not see an appreciable reduction in barrier
98 function as determined by transepithelial resistance, by 10 days of treatment we did
99 detect a reduction in aquaporin expression, increased photoreceptor cell outer segment
100 phagocytosis, and disruption of transcriptional profiles associated with fluid flux and ion
101 transport.
102
103 **RESULTS**
104 *Generation of hiPSC-derived RPE cells*
105 Donor fibroblasts were reprogrammed to human induced pluripotent stem cells
106 (hiPSCs) via Sendai virus mediated expression of the transcription factors OCT4,
107 SOX2, KLF4 and C-Myc as previously described (14). At 25-30 days following Sendai
108 viral transduction hiPSC colonies were manually isolated and clonally expanded in
109 Essential 8 media on laminin-521 coated cell culture surfaces. At passage 10 karyotypic
110 analysis was performed to ensure lack of chromosomal abnormalities (**Figure 1A**).
111 Following confirmation of normal karyotype, hiPSCs were differentiated into retinal
112 pigment epithelia (RPE) cells using the differentiation protocol developed by Foltz *et. al*.
113 (15). By 30 days of differentiation hiPSC-derived RPE cells formed a monolayer of
114 pigmented, polygonal cells with cobblestone morphology (**Figure 1B**). Expression of the
115 RPE genes *BEST1*, *MITF*, *RLBP1*, and *RPE65* were confirmed using RT-qPCR (**Figure**

116 **1C**). In addition, expression of the tight junction marker ZO-1 and transcription factor
117 PAX6 were confirmed via immunocytochemistry (**Figure 1D**).
118
119 *10 μM selumetinib optimally inhibits phosphorylation of MAPK in hiPSC-derived RPE*
120 To identify the dose of selumetinib suitable for suppressing MEK signaling without
121 inducing widespread cell death, an MTS cell viability assay was performed on the
122 hiPSC-RPE cells. In this experiment a $\log_{10}$-fold dilution of selumetinib ranging from
123 0.001 – 1000 μM was evaluated. hiPSC-RPE were treated for 72 hours before
124 absorbance at 490 nm was determined by a microplate reader. As shown in
125 **Supplementary Figure 2A**, cell viability dropped precipitously when selumetinib
126 concentrations exceeded 100 μM. To determine if selumetinib doses of 1 μM and 10 μM
127 (1 and 2 log units below the viability threshold) were sufficient to inhibit MEK signaling,
128 Western blot analysis using antibodies targeting the MEK effector MAPK
129 (**Supplementary Figure 2A**) was performed. While MAPK phosphorylation was
130 reduced in cells treated with 1 μM selumetinib, near complete inhibition of MAPK
131 phosphorylation was achieved using 10 μM selumetinib (**Supplementary Figure 2B**).
132 To determine the impact of selumetinib on MAPK phosphorylation as a function of
133 treatment time, hiPSC-derived RPE cells were evaluated following 10, 20, and 30 days
134 of treatment. Relative to untreated controls, hiPSC-derived RPE cells cultured in media
135 containing 10 μM selumetinib displayed significantly decreased MAPK phosphorylation
136 at all time points evaluated: Days 10 – 30 combined, 0.86 ± 0.083 vs 0.20 ± 0.206
137 (**Supplementary Figure 2C**); Day 10, 0.66 ± 0.11 vs 0.15 ± 0.033 (**Supplementary**

138 **Figure 2D**); Day 20, 0.71 ± 0.092 vs 0.15 ± 0.028 (**Supplementary Figure 2E**); and
139 Day 30, 1.2 ± 0.17 vs 0.31 ± 0.056 (**Supplementary Figure 2F**).
140
141 *Selumetinib does not affect transepithelial electrical resistance of hiPSC-derived RPE*
142 *cells*
143 If selumetinib disrupts the ability of RPE to maintain a monolayer of cells connected via
144 tight junctions, this could lead to non-selective movement of water and ions across the
145 blood-retinal barrier. The integrity of this barrier can be tested by measuring the
146 transepithelial electrical resistance (TEER) across a monolayer of RPE. Thus, to
147 evaluate TEER in our system, hiPSC-derived RPE were plated onto transwell inserts.
148 Beginning five days after plating (Day 0 on **Supplementary Figure 3**), cell media was
149 changed following treatment condition and TEER measurements were recorded every 3
150 days for up to 12 days with a final measurement at day 19 using the EVOM Meter
151 following the manufacturer's protocol. No significant difference in mean transepithelial
152 resistance was detected between untreated and selumetinib-treated hiPSC-derived
153 RPE cells at any of the time points evaluated (**Supplementary Figure 3**).
154
155 *Selumetinib treatment increases internalization of bovine rod outer segments by hiPSC-*
156 *derived RPE cells*
157 Another critical function RPE carry out to maintain retina homeostasis is phagocytosis of
158 photoreceptor outer segments. Diseases with disruptions to this process cause
159 blindness (16, 17). To determine if selumetinib treatment impacts the ability of RPE to
160 phagocytose photoreceptor outer segments, mature hiPSC-derived RPE cells cultured

161 in the presence or absence of 10 μM selumetinib were incubated for 3 hours with media
162 containing bovine rod outer segments (10 bROS/cell). Cells were subsequently washed
163 and collected as described below. The process of outer segment phagocytosis by the
164 RPE involves outer segment binding followed by internalization and lysosomal
165 degradation. The phagocytosis conditions that were collected for analysis in this
166 experiment included Total bROS (combined bound and internalized factions),
167 Internalized bROS (the portion of bROS inside the cell), and 3- and 24-hour Chase
168 conditions, which measure the amount of bROS present after allowing an additional 3-
169 or 24-hours of culture time following bROS washout (i.e. to allow for degradation). To
170 quantify bROS levels, western blot analysis for the rod outer segment protein rhodopsin
171 (RHO) was used (**Figure 2A**). Compared to untreated controls, selumetinib-treated
172 hiPSC-derived RPE cells were found to have significantly increased levels of
173 internalized RHO (**Figure 2B**, 1.879 ± 0.967 vs 2.972 ± 1.028, p=0.024). When
174 segregated by the number of days cells received treatment, we found the most
175 consistent increase was detected in cells treated for the first 10 days (**Figures 2C**, 0.7 ±
176 0.14 vs 1.6 ± 0.25, p=0.021). While not reaching statistical significance, increased RHO
177 abundance was still apparent following 20 days of treatment (**Figure 2D**, 1.3 ± 0.28 vs
178 2.7 ± 1.0, p=0.238). In the Day 30 treatment group, internalized RHO expression was
179 significantly higher in the selumetinib-treated cells (**Figure 2E**, 3.3 ± 3.0 vs 4.4 ± 3.1,
180 p=0.014). There was no statistically significant difference between treatment groups in
181 any of the other phagocytosis conditions evaluated at any individual time point or all
182 time points combined (**Figure 2C-E**). Collectively, these data demonstrate that
183 treatment of hiPSC-derived RPE cells with 10 μM selumetinib enhanced rod outer

184 segment phagocytosis but did not appear to alter clearance capacity (i.e., by just 3
185 hours following washout the levels of RHO inside the cells was not significantly different
186 between selumetinib treatment and control conditions).
187
188 *Selumetinib treatment decreases Aquaporin 1 (APQ1) expression in hiPSC-derived*
189 *RPE cells*
190 AQP1 is principally expressed apically in RPE cells and helps prevent and decrease
191 accumulation of subretinal fluid (18, 19). It has been shown to be regulated by the
192 MAPK pathway in these cells (20). Because of this, AQP1 is hypothesized to play a role
193 in MEKAR pathophysiology (5). To quantify changes in AQP1 protein expression
194 between untreated hiPSC-derived RPE and those treated for 10-, 20-, and 30-days,
195 western blot analysis was performed. When all treatment times were combined, we
196 detected a statistically significant decrease in AQP1 levels in the selumetinib-treated
197 hiPSC-derived RPE cells compared to untreated controls (**Figure 3A**, 1.6 ± 0.44 vs 0.98
198 ± 0.32, p=0.044). When the data was segregated by treatment time, it became evident
199 that the impact on selumetinib on AQP1 expression occurred within the first 10 days of
200 selumetinib treatment (**Figure 3B**, 2.7 ± 0.12 vs 1.1 ± 0.17, p=0.0015). Specifically, no
201 significant difference in AQP1 expression was found following 20- (**Figure 3C**, 1.6 ± 1.1
202 vs 1.4 ± 0.95, p=0.252) or 30-days of selumetinib treatment (**Figure 3D**, 0.46 ± 0.039 vs
203 0.43 ± 0.069, p=0.406).
204
205 *Selumetinib alters transcriptome of hiPSC-derived RPE*

206 Because our assays measured specific functions and proteins we hypothesized could
207 be affected by MEKAR pathophysiology, we decided to evaluate drug-induced changes
208 to the hiPSC-RPE transcriptome. This analysis allowed us to analyze the
209 pathophysiology in an unbiased nature and generate additional hypotheses regarding
210 the mechanism of MEKAR. Bulk RNA-sequencing revealed significant changes in
211 differentially expressed genes (DEGs) between untreated and selumetinib-treated
212 hiPSC-derived RPE cells (**Figure 4A-B**). Of the 9,360 genes with measured expression,
213 957 genes were differentially expressed between the treatment and no treatment control
214 groups. Notably, there was a significant decrease in all the top 50 DEGs associated with
215 small molecule and ion transport and lysosomal acidification (*LRRC8C, CLCN5,*
216 *SLC16A1, SLC6A6, SLC22A23, SL12A2, ATP6V1C2*) in selumetinib-treated hiPSC-
217 derived RPE (**Figure 4A-B, Supplementary Table 1**). Ingenuity pathway analysis
218 revealed the most significantly altered pathways were associated with neuroactive
219 ligand-receptor interactions, calcium signaling, PI3K-Akt signaling, and extracellular
220 matrix-receptor interaction (**Figure 4C**). Gene Ontology analysis revealed the top
221 biological processes altered between treatment conditions were associated with visual
222 perception, transport across the blood-brain barrier, and positive regulation of cytosolic
223 calcium ion concentration, peptidyl-tyrosine phosphorylation, and ERK1 and ERK2
224 cascade (**Figure 4D**). Treatment with selumetinib significantly altered gene expression
225 of several aquaporins: *AQP3, AQP4,* and *AQP7* increased and *AQP1* and *AQP11*
226 decreased in cells treated with selumetinib (**Supplementary Table 2**).
227
228 *Selumetinib does not alter hiPSC-derived RPE cell structure*

229 We imaged cultured cells to determine if selumetinib affects hiPSC-derived RPE cell
230 structure. Scanning electron microscopy (SEM) and transmission electron microscopy
231 (TEM) visualized the external and internal compartments of the cells, respectively. No
232 difference in cell structure was evident between untreated and selumetinib-treated
233 hiPSC-derived RPE cells (**Supplementary Figure 4**).
234

235 **DISCUSSION**

236 In the present study, we aimed to assess the effect of a commonly used MEK inhibitor,
237 selumetinib, on hiPSC-derived RPE cells *in vitro*. We found that treatment of hiPSC-
238 derived RPE with 10 μM selumetinib resulted in increased levels of internalized bovine
239 rod outer segments (bROS) and decreased aquaporin-1 (AQP1) protein expression
240 compared to untreated controls. These effects were most pronounced following 10 days
241 of treatment and appeared to decrease as treatment times increased, which is
242 consistent with clinical findings in patients with resolving MEKAR. Bulk RNA-sequencing
243 revealed significant changes in gene expression. Notably, there was a significant
244 decrease in expression of genes involved in transport of ions and small molecules
245 regulating cell volume and lysosomal acidification. We did not find an effect of
246 selumetinib on cell structure or the ability of hiPSC-derived RPE to maintain barrier
247 function as determined by transepithelial electrical resistance measurements.
248

249 *Selumetinib increases internalization of bovine rod outer segments by hiPSC-derived*
250 *RPE cells*

251 In a daily cycle, each rod photoreceptor cell sheds 10% of its membranous discs
252 contained within the photoreceptor outer segment. Shed outer segments are
253 phagocytosed by RPE cells where they are converted into fatty acids and ketone bodies
254 (13). Ketone bodies, primarily β-hydroxybutyrate (β-HB), are recycled back to the
255 subretinal space for use in metabolism by photoreceptor cells. In this study we found
256 that treatment of hiPSC-derived RPE cells with 10 μM selumetinib increased rod outer
257 segment phagocytosis. We predict that increased internalization and degradation of
258 photoreceptor outer segments leads to increased production and secretion of ketone
259 bodies into the subretinal space *in vivo*. This would be expected to contribute to
260 subretinal fluid accumulation characteristic of MEKAR. First, ketone anions attract
261 sodium and water (21). Second, β-HB has been shown to increase vascular
262 permeability via increased vascular endothelial growth factor (VEGF), which is the main
263 factor that can increases blood-retinal barrier permeability (22, 23). However, this
264 second mechanism is less likely to contribute to subretinal fluid accumulation in MEKAR
265 as vascular permeability has not been detected with fluorescein angiography (4, 5, 8-
266 10). Future work is needed to determine if MEK inhibitors increase ketone secretion by
267 RPE cells. If this is true, then increasing photoreceptor uptake of ketones may be a
268 reasonable process to target for treatment in patients with unresolving MEKAR. If future
269 animal studies confirm that drug-induced increases in RPE phagocytosis contribute to
270 MEKAR, reducing phagocytosis of shed outer segments or decreasing production of
271 ketones by RPE would not be recommended strategies for treatment as disruptions of
272 both processes are associated with blinding conditions such as age-related macular

273 degeneration (AMD), retinitis pigmentosa (especially those caused by mutations in
274 *MERTK*), and diabetic retinopathy (16, 17).
275
276 *Selumetinib treatment decreases expression of AQP1 in hiPSC-derived RPE cells*
277 Aquaporin 1 (AQP1) is a member of a family of transmembrane proteins that facilitate
278 water transport. It has documented expression and functionality in the RPE derived from
279 both human native tissue and differentiated from stem cells (18, 19). Because of its
280 localization to the apical cell surface, it transports water to the basolateral direction, thus
281 preventing subretinal fluid accumulation. Because of AQP1's location and role in the
282 RPE, it has been hypothesized that altered AQP1 may be responsible for causing
283 MEKAR (5). Our results support this hypothesis with 10 μM of selumetinib causing
284 decreased AQP1 protein expression following 10 days of selumetinib treatment. Bulk
285 RNA-sequencing data revealed that *AQP1* gene expression was also significantly
286 decreased in hiPSC-derived RPE treated with selumetinib (adjusted $p=2.95x10^{-4}$).
287 Interestingly AQP1 levels normalized by 20 days of treatment, which parallels the
288 clinical phenotype of patients who spontaneously resolve their MEK inhibitor-induced
289 subretinal fluid accumulation. Our results contrasts with findings reported by Jiang *et al.*
290 (20), in which they found that when ARPE-19 cells were treated with H2O2 or ultraviolet
291 radiation, MEK activation led to a decrease in AQP1 protein levels. In turn treating cells
292 with 1 μM of MEK inhibitor increased AQP1 expression. While both Jiang *et al.* and the
293 present study implicate MEK activity in regulating AQP1 levels in RPE cells, the
294 observed differences could be due to cell type (immortalized ARPE-19 cell line versus
295 hiPSC-derived RPE) or pharmacological MEK inhibitor (preclinical research-grade MEK

296 inhibitors PD98059 and U0126, versus clinically used selumetinib) (24). If future
297 research *in vivo* demonstrates that decreased AQP1 contributes to MEKAR, a potential
298 treatment for affected patients may be administration of agents that increase water
299 transport via AQP1. For instance, drugs such as atrial naturietic peptide (ANP) or
300 membrane-permeable analogs of cyclic GMP (cGMP), which Baetz *et al*. found
301 significantly increase net fluid flux (25), may be useful for preventing MEKAR. Topical
302 and oral administration of carbonic anhydrase inhibitors may be another potential
303 therapeutic as its use decreases subretinal fluid in conditions such as central serous
304 chorioretinopathy, retinitis pigmentosa, and X-linked retinoschisis (26-33). While the
305 mechanism is unclear, it is thought to restore apical-to-basal fluid transport across RPE
306 cells by acidifying the subretinal space (27, 29, 34, 35).
307
308 *Selumetinib decreases expression of genes regulating small molecule and ion transport*
309 *as well as lysosomal acidification*
310 The most striking difference in RNA-sequencing data between untreated and
311 selumetinib-treated cells was the significant decrease in expression of genes involved in
312 transport of ions and small molecules as well as those involved in lysosomal
313 acidification (**Supplementary Table 1**). Depending upon the polar distribution of the
314 affected genes' protein products, the observed decrease in expression may be a direct
315 effect of treatment with selumetinib or a cellular compensation (36).
316
317 *LRRC8C* codes for a subunit of the LRRC8 which is a volume-regulated anion channel
318 (VRAC) (37). It contributes to cell volume homeostasis via its expression on the plasma

319 membrane. When cells swell, this channel is activated and allows efflux of charged and
320 uncharged molecules. However, regulatory volume decrease (RVD) is mainly mediated
321 by efflux of potassium, chloride, and H2O. VRACs like LRRC8 primarily efflux chloride
322 ions. LRRC8 has also been shown to be expressed on lysosomes, the “osmometer” of
323 mammalian cells (38). LRRC8 contributes to lysosomal currents and is necessary to
324 form large lysosome-derived vacuoles which store and eliminate water via exocytosis.
325 In this way, they further maintain H2O balance intracellularly and have been described
326 as the “bladder” of the cell. While the polarized localization of LRRC8 within the RPE
327 cell has not been documented, decreased expression of *LRRC8C* in selumetinib treated
328 hiPSC-derived RPE cells may prevent formation of these water-filled vacuoles, leading
329 to apical fluid accumulation. Additionally, decreased expression of *LRRC8C* may be a
330 cellular compensatory mechanism to inhibit efflux of chloride and water apically or the
331 subretinal space *in vivo*.
332
333 *CLCN5* codes for ClC-5, which is a chloride-hydrogen exchanger with documented
334 function acidifying lysosomes and up-taking protein in the proximal tubule cells (PTCs)
335 of the kidney (39). Mutations in *CLCN5* cause Dent disease, a proximal tubulopathy of
336 the kidney characterized by high levels of protein and calcium excreted in the urine,
337 contributing to kidney stone formation. In PTCs, ClC-5 interacts with proteins important
338 for receptor-mediated endocytosis and transportation to lysosomes for metabolism. Its
339 expression on the cell membrane is thought to contribute to chloride currents. Polarized
340 localization within RPE cells has not been documented. Decreased *CLCN5* expression
341 in selumetinib-treated hiPSC-derived RPE could contribute to decreased lysosome

342 acidification and may be a compensatory mechanism to prompt absorption of fluid by
343 acidifying the subretinal space (35).
344
345 *SLC16A1* encodes MCT1, a $H^+$-coupled monocarboxylate transporter that transports
346 lactate into the cell (40). Due to its coupling with hydrogen ions, it contributes to
347 intracellular acidification in addition to fluid transportation. MCT1 is highly expressed on
348 the apical surface of RPE cells to facilitate uptake of metabolic waste products from
349 overlying photoreceptors (40-42). Thus, decreased expression of MCT1 protein on the
350 apical surface of RPE treated with selumetinib could contribute to decreased
351 acidification intracellularly and accumulation of protons in the subretinal space. While
352 protons attract water molecules, acidification of the subretinal space may prompt fluid
353 transport across RPE cells and thus serve as a compensatory mechanism (35).
354
355 *SLC6A6* codes for a sodium- and chloride-dependent transporter (TauT) of taurine and
356 beta-alanine localized to the plasma membrane (43, 44). Taurine is highly abundant in
357 the retina, particularly in photoreceptors at the level of the outer nuclear layer. It is
358 necessary for proper retinal structure and function with low levels associated with retinal
359 degeneration at the level of the photoreceptors in animal models and humans (45-47).
360 TauT is a well-known contributor to osmoregulation, whereby hypertonic extracellular
361 conditions lead to intracellular influx of taurine and obligate water molecules mediated
362 by transporters like TauT. TauT protein is expressed at similar levels in apical versus
363 basolateral sides of human fetal RPE cells (48). Activity and gene and protein
364 expression of TauT is increased in ARPE-19 cells following exposure to hyperosmolar

365 media (46). Decreased expression of *SLC6A6* in selumetinib-treated cells may been a
366 compensatory mechanism whereby cells with increased internalized POS decrease the
367 amount of osmotically active taurine influx to prevent cell swelling. Thus, decreased
368 permeability to taurine and water could lead to an accumulation of these molecules in
369 the subretinal space.
370
371 *SLC22A23* encodes one of the ~30 members in the highly conserved SLC22 transporter
372 family (49). Its protein product's function and structure have not been well-
373 characterized. However, evolutionary analysis indicates that it likely functions as an
374 organic anion transporter (OAT) and contributes to metabolic regulation. More work is
375 needed to determine the effect of decreased *SLC22A23* observed in selumetinib-treated
376 hiPSC-derived RPE cells.
377
378 *SLC12A2* encodes NKCC1, a $Na^+$-$K^+$-$Cl^-$ cotransporter that mediates influx of chloride in
379 an electrically neutral transfer, which contributes to cell volume regulation (50, 51). Its
380 expression is localized to the basolateral membrane of chloride-secreting epithelial cells
381 except in the olfactory epithelium, choroid plexus, and RPE, where is localized on the
382 apical membrane (51-55). NKCC1 regulates subretinal fluid volume via ion transport
383 (51). Because of its apical location, it transports chloride and therefore H2O out of the
384 subretinal space in the basolateral direction. Thus, decreased expression of NKCC1 in
385 selumetinib-treated hiPSC-derived RPE could decrease chloride and water transport
386 from the apical surface and contribute to subretinal fluid accumulation.
387

388 *ATP6V1C2* encodes for a subunit of vacuolar ATPase (V-ATPase), a highly conserved
389 proton pump which acidifies intracellular organelles, including lysosomes (56, 57). It
390 hydrolyzes ATP to drive protons across a membrane. Specificity of localization in
391 organelles and cell and tissue type are determined by isoforms of subunits. *ATP6V1C2*
392 encodes for the V1C2 isoform. V-ATPases are found ubiquitously in the
393 endomembranes of organelles and in the plasma membranes of certain cell types
394 including osteoclasts, renal intercalated cells, male reproductive tract epithelial cells,
395 and tumor cells. Multiple diseases are associated with mutations, mis-localization, and
396 overexpression of V-ATPase subunits (57). Notably, a potentially pathogenic mutation
397 was identified in *ATP6V1C2* (58). The missense mutation causing loss-of-function on V-
398 ATPase was found with whole-exome sequencing in a patient with distal renal tubular
399 acidosis. V-ATPases are found on the apical side of $\alpha$-intercalated cells in the distal
400 nephron and acidify urine. (57, 59). *ATP6V1C2* expression in RPE is documented (60-
401 64). Animal models with inhibition or mutations of V-ATPases in the lysosomes of RPE
402 cells impairs phagocytosis and degradation of photoreceptor outer segments (65-67).
403
404 *Selumetinib alters gene expression of aquaporins*
405 Aquaporins are a family of membrane channels permeable to water. Treatment of
406 hiPSC-derived RPE with selumetinib significantly altered gene expression of several
407 aquaporins with confirmed expression in hiPSC-derived RPE: *AQP1, AQP3, AQP4,*
408 *AQP7,* and *AQP11* (**Supplementary Table 2**) (19). Expression of *AQP1* and *AQP11*
409 were increased, whereas expression of *AQP3, AQP4,* and *AQP7* decreased.
410 Interestingly, MAPK pathway activation helps cells cope with osmotic stress (68). Thus,

411 inhibition of this pathway with selumetinib could potentially disrupt RPE cells' ability to
412 adapt to subretinal fluid accumulation by altering transcription of aquaporin genes.
413 Notably, the ionic and osmotic composition of MEKAR-associated subretinal fluid has
414 not been characterized. Regardless, alterations in expression of aquaporins in RPE
415 cells due to MEK inhibition could certainly contribute to subretinal fluid accumulation.
416
417 While AQP3 protein expression has been confirmed in primary RPE cells, the polarized
418 cellular localization has not been reported (69). Our results showed that MEK inhibition
419 with selumetinib significantly increased *AQP3* expression in hiPSC-derived RPE. This
420 contrasts with what Hollborn *et al*. found (69). They reported increased AQP3 mRNA
421 induced by MEK activation in primary human RPE cells treated with CoCl2 to chemically
422 induce hypoxia. To determine that this change in AQP3 expression was mediated by
423 MEK activation, they inhibited MEK with the preclinical, research-use only molecule
424 PD98059 (20 μM), whereas our study used selumetinib which is used in clinical practice
425 to treat patients (24). Future work is needed to determine the cellular localization of
426 AQP3 to the apical and/or basolateral side of RPE and if there are differences in the
427 changes in AQP3 expression with MEK modulation in different types of RPE cell
428 cultures (primary versus stem-cell derived) and with different MEK inhibitors.
429
430 Our study found AQP4 gene expression significantly increased in hiPSC-derived RPE
431 treated with selumetinib. The polar cellular location of AQP4 in RPE has not been
432 documented. Perhaps increased expression in selumetinib-treated cells is a
433 compensatory mechanism to transport water out of the subretinal space into the choroid

434 underlying the RPE. This differs from a study in ARPE-19 cells where inhibition of
435 MAPK with 10 μM UO126 did not rescue decreased AQP4 protein expression in
436 response to hyperosmolar conditions (70).
437
438 Like AQP3, AQP7 is also permeable to small solutes like glycerol and exhibited
439 increased gene expression in hiPSC-derived RPE cells treated with selumetinib. AQP7
440 enables efflux of glycerol, thus increased AQP7 could allow for accumulation of glycerol
441 and water in the subretinal space (71, 72).
442
443 Similar to *AQP1* gene expression in hiPSC-derived RPE treated with selumetinib, levels
444 of AQP11 mRNA decreased. Research on Müller glia cells have demonstrated an
445 association between intracellular edema and decreased AQP11 levels of activity
446 contributing to Diabetic Macular Edema (DME) characterized by subretinal and
447 intraretinal fluid accumulation (73). If AQP11 proteins behave the same way in RPE
448 cells, then perhaps decreased expression in selumetinib-treated cells prevents water
449 efflux. This increase in cell swelling may then prevent increased intracellular uptake of
450 water, contributing to subretinal fluid accumulation.
451
452 *Comparison of MEKAR to ocular phenotypes caused by mutations in BEST1*
453 *BEST1* encodes a membrane protein that acts as a cell volume-sensitive calcium-gated
454 chloride channel which inhibits voltage-gated calcium channels (74, 75). While it is
455 predominantly expressed in human RPE, it has also been detected in the kidney, brain,
456 spinal cord, and testis (76, 77). Within the RPE, it is localized to the basolateral

457 membrane and exhibits higher expression levels outside of the macula (78, 79).
458 Interestingly, bestrophin protein is also suspected to regulate intracellular calcium and
459 processes like phagocytosis and lysosomal function (80, 81). As demonstrated in this
460 study, calcium signaling and regulation of cytosolic calcium concentrations were some
461 of the top pathways affected in hiPSC-derived RPE cells. Pathologic mutations in
462 *BEST1* can cause a spectrum of ocular phenotypes, mostly leading to detachment of
463 the neurosensory retina at the macula with accumulation of subretinal fluid, causing a
464 decrease in visual acuity (74). Notably however, this decrease in visual acuity is not
465 large and many patients remain stable without treatment at 20/50. Like MEKAR, it is
466 hypothesized that accumulation of fluid in the subretinal space in *BEST1*-associated
467 diseases is due to dysfunction of RPE's ability to transport ions and regulate fluid
468 homeostasis including via phagocytosis of photoreceptor outer segments (POS). In
469 contrast to MEKAR, it is thought that *BEST1* mutations modulating intracellular calcium
470 levels may decrease uptake of POS, leading to accumulation of toxic lipofuscin in the
471 subretinal space, killing both photoreceptors and RPE cells. Lipofuscin is a mixture of
472 byproducts form POS degradation and includes oxidized proteins, lipids, and
473 fluorophores. A study using hiPSC-derived RPE cells from patients with Best disease
474 and non-affected siblings produced results that supported this hypothesis (82). They
475 found cells from affected patients demonstrated decreased apical to basal fluid flux,
476 increased accumulation of lipofuscin after feeding POS, decreased degradation of
477 rhodopsin (RHO) after POS feeding, and differential responses to calcium stimulation. It
478 is unknown whether lipofuscin accumulation is a feature of MEKAR. Given the clinical
479 similarities between MEKAR and *Best1*-associated ocular diseases (eg, bilateral

480 accumulation of subretinal fluid predominantly at the macula, decreased visual acuity,
481 and affected proteins involved in ion transport, volume sensation and regulation, POS
482 phagocytosis, and lysosomal acidification), future work should address the possibility of
483 overlapping disease mechanisms.
484
485 *Conclusion*
486 In summary, using an *in vitro* model of MEKAR, we have shown that the clinically used
487 MEK inhibitor, selumetinib increases hiPSC-derived RPE cell phagocytosis, decreases
488 AQP1 mRNA and protein, and alters gene expression with significant changes in genes
489 involved in transport of ions and small molecules regulating cell volume and lysosomal
490 acidification. Increased phagocytosis could potentially increase return of ketones to the
491 subretinal space while decreased AQP1 protein expression would prevent water
492 transport out of the subretinal space. This decrease is AQP1 may be a cellular response
493 to prevent cell swelling of RPE accumulating internalized photoreceptor outer segments
494 and their metabolites intracellularly. Thus, theoretically both increased phagocytosis and
495 decreased AQP1 could contribute to the subretinal fluid accumulation characteristic of
496 MEKAR. Future work is needed to further investigate these hypotheses and the roles of
497 genes involved in lysosome acidification and cell volume regulation via molecular and
498 ionic transport in the context of MEKAR.
499
500 *Future Directions*
501 More work is needed to further assess whether the MEK inhibitor-induced increase in
502 hiPSC-derived RPE cell phagocytosis affects the rate of ketone recycling into the

503 subretinal space. This could be achieved using mass spectrometry on apical and basal
504 cell culture media following the phagocytosis assays. This has been documented as the
505 most reliable method to quantify secreted β-hydroxybutyrate (β-HB), the predominant
506 ketone, from cultured human fetal RPE cells (83). Additionally, monocarboxylate
507 transporter isoform 1 (MCT1) permits secretion of β-HB and is located on the apical side
508 of RPE cells (84). Thus, quantification of MCT1 could also provide insight into an
509 increased ability of ketone bodies to leave RPE cells and travel into the subretinal
510 space. This would be especially interesting to quantify given that our RNA-sequencing
511 data showed a significant decrease in *SLC16A*, the gene encoding MCT1.
512
513 This study assessed the effect of selumetinib on mRNA expression levels. There is
514 precedent in the literature to evaluate changes in total RNA in future studies given the
515 role of microRNAs (miR) in regulating phagocytosis (85). Specifically, miR-302d
516 suppresses phagocytosis in cultured cells from the ARPE-19 cell line (86). Additionally,
517 other miRs are reported to alter RPE autophagy (85). Thus, future work could quantify
518 the impact of MEK inhibitors on microRNAs in cultured RPE cells.
519
520 Finally, the MEK inhibitor-induced differences in gene expression revealed in this study
521 warrant further exploration. Specifically, work is needed to investigate if genes with
522 altered expression play a role in the observed changes in hiPSC-derived RPE cell
523 functions. For example, osmotic challenge assays and imaging can assess the effect of
524 selumetinib on fluid flux and cell volume (18, 36).
525

526 **METHODS**

527 *Sex As a Biological Variable*

528 Cells from a single male donor were used in this study. There is no evidence to suggest
529 that there is a sex difference in patients affected with MEKAR.

530

531 *Creation and Maintenance of Human Induced Pluripotent Stem Cell Cultures*

532 Induced pluripotent stem cells were generated from a dermal biopsy of an unidentifiable
533 male donor as previously described by Wiley *et al*. (14). All cell types were cultured at
534 37C, 5% CO2, and 20% O2. Briefly, fibroblasts were isolated and expanded from a 3
535 mm dermal biopsy and transduced with CytoTune-iPSC 2.0 Sendai Reprogramming Kit
536 (Invitrogen/Thermo Fisher Scientific, Waltham, MA, USA). hiPSC colonies were isolated
537 and expanded. TaqMan Human Pluripotent Stem Cell Scorecard Panel (Life
538 Technologies/Thermo Fisher Scientific, Waltham, MA, USA) was used to analyze
539 pluripotency and loss of viral transgene expression. Karyotype analysis was carried out
540 by the University of Iowa Shivanand R. Patil Cytogenetic and Molecular Laboratory
541 following a standard G-banding protocol.

542

543 *Differentiation and Maintenance of hiPSC-derived Retinal Pigment Epithelial Cells*

544 We followed the rapid, directed differentiation protocol by Foltz and Clegg (15). The
545 ROCK-inhibitor Y-27632 (MilliporeSigma, Burlington, MA, USA) was added to cell
546 media at each passage for 4-7 days to increase cell survival and attachment. Briefly,
547 hiPSCs were grown to 80% confluence in Essential 8 Flex media (Gibco/Thermo Fisher
548 Scientific, Waltham, MA, USA) on rhLaminin-521 (Gibco/Thermo Fisher Scientific,

549 Waltham, MA, USA) coated plates and then passaged with ReLeSR™ (STEMCELL
550 Technologies, Vancouver, BC, Canada) 1:4 onto Matrigel-coated plates and treated for
551 14 days with growth factors. After RPE expansion, cells were maintained in RPE
552 Supporting Media (RSM), composed of X-VIVO 10 (Lonza, Basal, Switzerland) and
553 0.2% Primocin (InvivoGen, San Deigo, CA, USA) on tissue culture-treated plates coated
554 with Matrigel (60 ug/ml; Corning Life Science, Tewksbury, MA). Following the ROCK
555 inhibition-dependent extended passage protocol by Croze, Bucholz, Radeke *et al*.(87),
556 cells were passaged after reaching confluence every 4-5 days with TypLE™ Express
557 (Thermo Fisher Scientific, Waltham, MA, USA) and plated at a seeding density of
558 $2.5x10^4$ cells/$cm^2$. Only cells at or below passage 5 were used to avoid epithelial-to-
559 mesenchymal transition and loss of RPE morphology (e.g., pigment, cobblestone
560 appearance) (87). Once cells were seeded onto experimental plates at density of
561 $1.0x10^5$ cells/$cm^2$ they were allowed to mature for 30 days before drug treatment, unless
562 otherwise specified (e.g. TEER assay).
563
564 *Pharmacologic Inhibitor of the MAPK/ERK Pathway*
565 Selumetinib (MEK inhibitor) was reconstituted to 10 mM in DMSO (Fisher Chemical,
566 Hampton, NH, USA) per the manufacturer's recommendations (Sigma-Aldrich, St.
567 Louis, MO, USA).
568
569 *MTS Assay*
570 To determine the maximum dose of selumetinib that could be applied to hiPSC-derived
571 RPE cells without causing cell death, cells were plated in Matrigel-coated 96-well

572 black/clear bottom plates (Corning Life Science, Tewksbury, MA) in X-VIVO 10. hiPSC-
573 derived RPE were plated at $1.0x10^5$ cells/$cm^2$ and allowed to mature for 30 days before
574 starting drug treatment. Cells were treated with a $log_{10}$-fold dilution from $1.0 \times 10^{-3}$ – 1.0
575 x $10^3$ uM selumetinib for 3 days in media free of antibiotics. After 72 hours of treatment,
576 selumetinib-free media was added to the cells along with 20 ul of CellTiter 96® $AQ_{queous}$
577 One Solution per well as directed in the manufacturer's instructions (Promega, Madison,
578 WI, USA). After 3 hours of incubation with MTS, the absorbance at 490 nm of each well
579 was measured using the BioTek Cytation 5 microplate reader (Agilent Technologies,
580 Santa Clara, CA, USA).
581
582 *Quantitative Real-Time Polymerase Chain Reaction (RT-qPCR)*
583 cDNA was generated from 200 ng RNA using SuperScript IV VILO Master Mix (Thermo
584 Fisher Scientific, Waltham, MA, USA). PCR reactions were run using PrimeTime™
585 qPCR probes (Integrated DNA Technologies, Coralville, Iowa, USA) and TaqMan™ Fast
586 Advanced Master Mix (Thermo Fisher Scientific, Waltham, MA, USA). cDNA was
587 amplified using a QuantStudio 6 Flex Real-Time PCR system (Thermo Fisher Scientific,
588 Waltham, MA, USA). Data were analyzed using delta-delta Ct method in which values
589 were normalized to the *B2M* housekeeping gene and corresponding mRNA values in
590 hiPSCs from the same donor.
591
592 *Immunocytochemistry (ICC)*
593 Cells were seeded onto 12-mm round glass coverslips coated in poly-L-lysine (Corning
594 Life Science, Tewksbury, MA) and Matrigel which were placed in 24-well tissue culture

595 treated plates (Corning Life Science, Tewksbury, MA). Cells were fixed with 4%
596 paraformaldehyde for 20 minutes at room temperature then blocked for 1 hour. Cells
597 were incubated with primary antibody for 2 hours at room temperature or overnight at
598 4C. Cells were washed with1xDPBS before incubating with secondary antibody and
599 1:2000 DAPI (Thermo Fisher Scientific, Waltham, MA, USA) for 1-2 hours at room
600 temperature. Cells were washed then mounted onto microscope slides with coverslips
601 and imaged at 40x using a Leica TCS SPE upright confocal microscope system (Leica
602 Biosystems, Wetzlar, Germany). Primary and secondary antibody details shown in
603 **Supplementary Table 3**.
604
605 *Transepithelial Electrical Resistance Assay (TEER)*
606 Cells were seeded onto 6.5 mm cell culture inserts (Corning Life Science, Tewksbury,
607 MA) coated with Matrigel. Five days after plating, cells were treated with 10 uM
608 selumetinib for a total of 20 days. Resistance measures were obtained every 3 days
609 using the EVOM Meter following the manufacturer's protocol (World Precision
610 Instruments, Sarasota, FL, USA). The resistance value of a cell culture insert without
611 cells was subtracted from all sample resistance measurements.
612
613 *Rod Outer Segment Phagocytosis Assay*
614 Bovine rod outer segments (bROS) (InVision BioResources, Seattle, WA, USA) at a
615 concentration of 10 bROS/cell were added to hiPSC-derived RPE cells in a volume of
616 500 ul/well of a 24-well plate. Cells were incubated with bROS for 3 hours at 37C and
617 5% CO2. After 3 hours, all conditions were washed five times with 1xDPBS with calcium

618 and magnesium. Prior to these washes, wells for the Internalized bROS condition were
619 incubated with 2 mM EDTA in PBS for 10 minutes at 37C, 5% CO2 to remove unbound
620 bROS. After washes, Total and Internalized condition wells were collected. 3 h and 24 h
621 Chase conditions received fresh media with or without selumetinib per treatment group.
622 At Chase collection time, cells were washed twice with 1xDPBS. Before collecting cells
623 from any condition, 10 uM recombinant human FGF-basic (Peprotech/Thermo Fisher
624 Scientific, Waltham, MA, USA) was added for a 10 minute incubation at 37C, 5% CO2.
625 This step was done to ensure visualization of Ph-MAPK on Western Blot.
626
627 *Scanning Electron Microscopy*
628 Cells were seeded onto 6.5 mm cell culture inserts (Corning Life Science, Tewksbury,
629 MA). At Day 10 of treatment, cells were fed bROS and incubated for 3 hours at 37C and
630 5% CO2. Cells were fixed with 2.5% glutaraldehyde for 3-5 days then rinsed with
631 1xPBS. Samples were post fixed for 1 hour with 1% osmium tetroxide and rinsed with
632 $ddH_2O$. The samples underwent alcohol series dehydration followed by chemical drying
633 with hexamethyldisilazane and left to dry in the fume hood for ≥ 2 days. Plates and
634 membranes were mounted with colloidal silver onto standard SEM stubs and dried
635 overnight. Sputter coating deposition was performed for 4 minutes with a current of
636 7mA. Coverslips were imaged on the Hitachi S-4800 at the Central Microscopy
637 Research Facility.
638
639 *Transmission Electron Microscopy (TEM)*

640 Cells were seeded onto 6.5 mm cell culture inserts with 0.4 um pore size (Corning Life
641 Science, Tewksbury, MA). At Day 10 of treatment, cells were fixed overnight in ½
642 strength Karnovsky's fixative. After primary fixation, samples were post fixed in osmium
643 tetraoxide and uranyl acetate, and were dehydrated through a graded series of
644 alcohols, acetone, and finally propylene oxide. The samples were then embedded in
645 Spurr's resin and cured at 60°C. After samples were fully cured ultrathin sections were
646 collected onto copper square mesh grids using an ultramicrotome. Samples were
647 imaged on the Hitachi HT7800 at the Central Microscopy Research Facility.
648
649 *Western Blot Analysis*
650 Cells cultured and treated on 24-well plates were collected then lysed with 75 ul RIPA
651 Lysis and Extraction Buffer with 1:100 Halt™ Phosphatase and Proteinase Cocktail
652 Inhibitors (Thermo Fisher Scientific, Waltham, MA, USA). Protein concentration was
653 quantified using Pierce™ BCA Protein Assay(Thermo Fisher Scientific, Waltham, MA,
654 USA) with duplicates of 10 ul per standards and samples. Colorimetric changes in
655 plates were read at 562 nm with the BioTek Cytation 5 microplate reader after 30
656 minutes of incubation at 37C. 10 ug protein was run on a 4-20% Novex™ Tris-Glycine
657 gel (Thermo Fisher Scientific, Waltham, MA, USA) for 25 minutes at 225 volts. Broad-
658 range protein transfer to blots was performed using iBlot™ 3 set to a 6 minute run at 25
659 volts with low cooling (Thermo Fisher Scientific, Waltham, MA, USA). After incubation
660 with blocking buffer for 1 hour at room temperature or overnight at 4C, blots were
661 probed with primary antibody then washed and probed with HRP-conjugated secondary
662 antibody (as shown in **Supplementary Table 4**). Blots were imaged using the iBright™

663 FL1500 (Thermo Fisher Scientific, Waltham, MA, USA). Blots were then stripped with
664 Restore™ stripping buffer (Thermo Fisher Scientific, Waltham, MA, USA) and probed
665 for beta-actin after imaging to confirm stripping removed previously bound antibody for
666 protein of interest. Densitometry was performed in FIJI ImageJ. All protein bands were
667 normalized to beta-actin.
668
669 *Gene Expression Profiling Using RNA-Sequencing*

670 RNA from cells was isolated using the NucleoSpin RNA kit (Machery-Nagel, Düren,
671 Germany) and final samples were eluted in 40 ul of RNAse free water. Gene expression
672 profiling using RNA-Seq was performed by the University of Iowa Genomics Division
673 using manufacturer recommended protocols. Briefly, 250 ng of DNase I-treated total
674 RNA was used to prepare sequencing libraries using the Illumina stranded mRNA
675 library preparation kit (Illumina, Inc., San Diego, CA, USA).

676 The pooled and barcoded libraries were sequenced on the Element AVITI24
677 sequencing platform (Element Biosciences, San Diego, CA) using a Cloudbreak FS 150
678 cycle (2x75 bp) high output sequencing flow cell to generate at least 30M paired-end
679 sequencing reads per sample.

680 *Bulk RNA Sequencing Analysis*

681 Data were processed using the nf-core/rnaseq pipeline v3.18.0; doi:
682 10.5281/zenodo.1400710 from the nf-core workflow collection (88), utilizing
683 reproducible software environments from the Bioconda (89) and Biocontainers (90)
684 projects. The pipeline was executed with Nextflow v24.10.5 (91). In brief, paired-end

685 sequence reads were pre-processed by Trim Galore v0.6.10 (92)using Cutadapt v4.9
686 (93) to remove adapter sequences and filter low quality reads. Both raw and trimmed
687 FASTQ files (94) were evaluated for quality control using FastQC v0.12.1 (95) to assess
688 Phred scores, GC content, sequence length distributions, and identify over-represented
689 sequences. Lightweight pseudo-alignment and quantification was completed using
690 Salmon v1.10.3 (96) with the selective alignment mapping strategy (97). A
691 transcriptome index was constructed from Ensembl *Homo sapiens* primary assembly
692 GRCh38 by generating a decoy-aware transcriptome for k-mers of length 31 from gene
693 transfer format (GTF) genome annotations (release 113) and the full reference genome
694 sequence. Paired-end reads were then quantified in mapping-based mode for inward
695 reverse strand-specific libraries.

696 Quantification results were analyzed using R ((98); R version 4.4.1 (2024-06-14)) and
697 several Bioconductor packages v3.20.0 (99). Transcript-level quantification results
698 output by Salmon were summarized to gene-level abundance estimates and read
699 counts (100) using tximeta v1.24.0 (101) with a linked transcriptome to the Ensembl
700 GRCh38 reference genome. Additional gene annotations were obtained using
701 AnnotationDbi v1.68.0 (102) and org.Hs.eg.db v3.20.0 (103). Exploratory data analysis
702 was facilitated by data structures and methods from the SummarizedExperiment
703 v1.36.0 (104) and tidybulk v1.18.0 (105) packages. Analysis of differential expression
704 was limited to samples from day 10, 20, and 30 time points. Low count genes were
705 excluded following (106), setting a minimum count-per-million threshold of 10 for a
706 minimum group size of 3. Fold change estimates and p-values were calculated using
707 DESeq2 v1.46.0 (107) by fitting a negative binomial generalized linear model with a

708 Wald test to assess coefficient significance. To identify treatment-driven gene
709 expression changes, an additive model was specified to account for batch (1, 2, or 3)
710 and treatment (10 μM vs. 0 μM) effects (108). Pathway analysis was conducted with
711 iPathwayGuide using BH-adjusted *p*-values with differential expression thresholds of
712 0.05 for genes with absolute $\log_2$ fold changes > 1 (109).

713 *Statistics*

714 Statistical analysis was performed in GraphPad Prism Version 10.2.3 (347) unless
715 otherwise noted. All data were collected from three independent experiments (n=3).
716 Statistical significance was calculated using paired t-test for all RPE cell function assays
717 (alpha = 0.05, FDR = 0.01).

718 *Study Approval*

719 Cell obtained from an anonymous donor, exempt from human subjects approval.

720 *Data Availability*

721 Data is available on Gene Expression Omnibus (GEO): accession number GSE308550.

722

723

724

725

726

727

728

729

730

731 **AUTHOR CONTRIBUTIONS**

732 LPL, RFM, EMB, and BAT conceptualized the study, devised methodology, and
733 generated figures. LPL conducted experiments, performed formal analysis, and wrote
734 the original draft. JAR performed formal analysis, generated figures, and submitted data
735 to Genome Expression Omnibus. LPL, MJ, RJ, LAW, BH, MJR, and ATW acquired
736 data. RFM, EMB, BAT, BAE, HCB and TMB reviewed and edited the manuscript. RFM,
737 EMB, and BAT provided resources and supervised the study. EMB and BAT acquired
738 funding.

739

740

741

742

743

744

745

746

747

748

749

750

751

752

753

**FUNDING SUPPORT**

US National Institutes of Health (NIH): T32 GM139776, funding Lola Lozano.

Gilbert Family Foundation: Development of novel next generation systems for study and treatment of NF1, funding Tucker Stem Cell Laboratory.

**ACKNOWLEDGEMENTS**

The authors thank the patient for their tissue donation and generosity in supporting biomedical research. This work was funded by the Gilbert Family Foundation, P30 EY025580, and the University of Iowa Medical Scientist Training Program (T32 GM139776). Data presented herein were obtained at the Genomics and Bioinformatics Divisions of the Iowa Institute of Human Genetics (RRID: SCR_023422) which is supported, in part, by the University of Iowa Carver College of Medicine. We would like to thank the directors of each of these divisions for their guidance, Kevin Knudtson and Michael Chimenti, respectively. We offer particular thanks to Mary Boes who performed bulk RNA-sequencing. We also would like to thank the Central Microscopy Research Facility for providing instrumentation for scanning and transmission electron microscopy. Figures generated with BioRender.

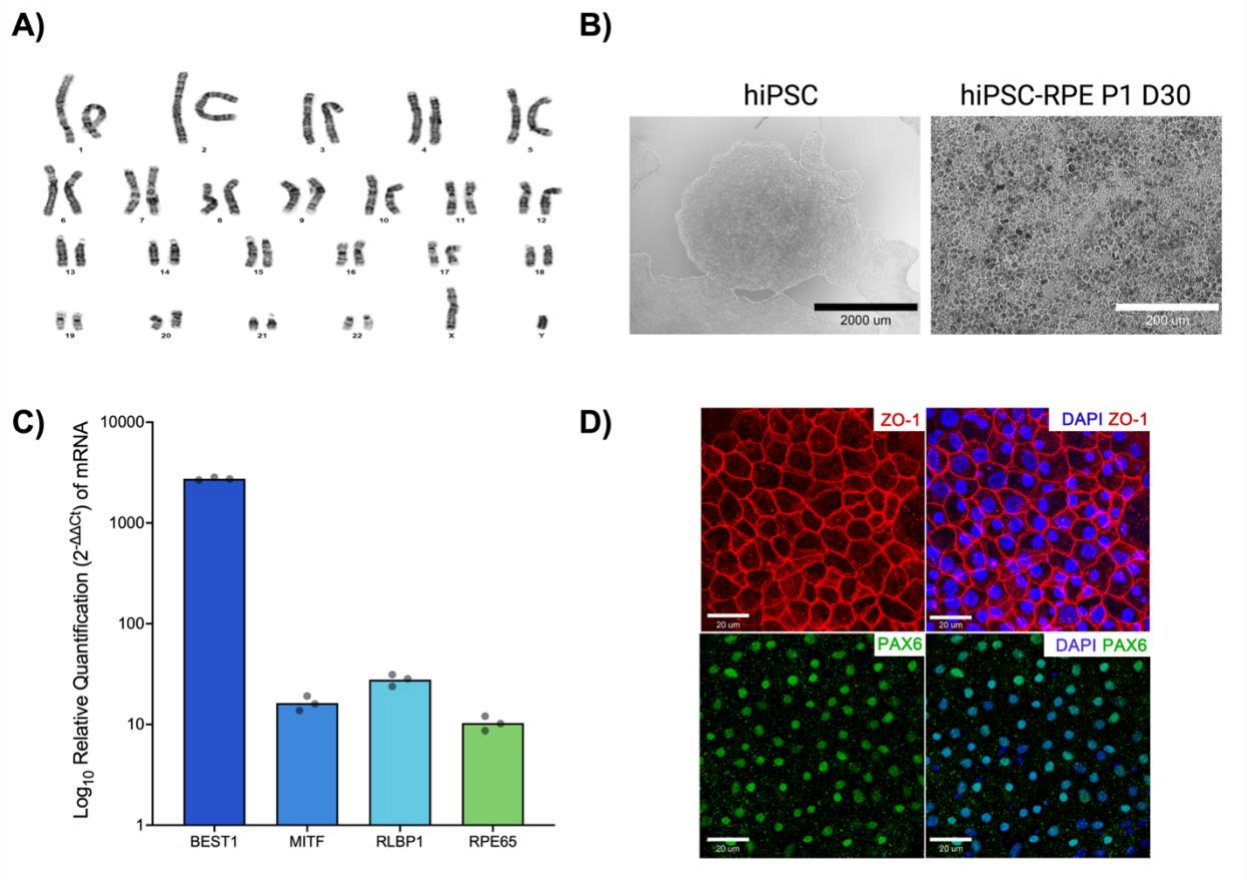


**Figure 1 - Differentiation of hiPSCs into RPE. A)** Normal karyotype after reprogramming donor fibroblasts into human induced pluripotent stem cells (hiPSCs). **B)** hiPSCs display typical translucent colonies composed of densely packed cells. After differentiation to hiPSC-derived RPE, the cells form a cobblestone-like monolayer of pigmented polygonal cells, morphology characteristic of RPE cells. **C)** RT-qPCR for signature RPE genes. delta-delta Ct values with bar height at the mean of technical triplicates. Values are normalized to the housekeeping gene *B2M* and values from hiPSCs derived from the same donor. **D)** Immunocytochemistry for signature RPE proteins. Cell membranes label strongly for the tight junction protein, ZO-1, while nuclei show robust labeling for PAX6, a key protein in eye specific development.

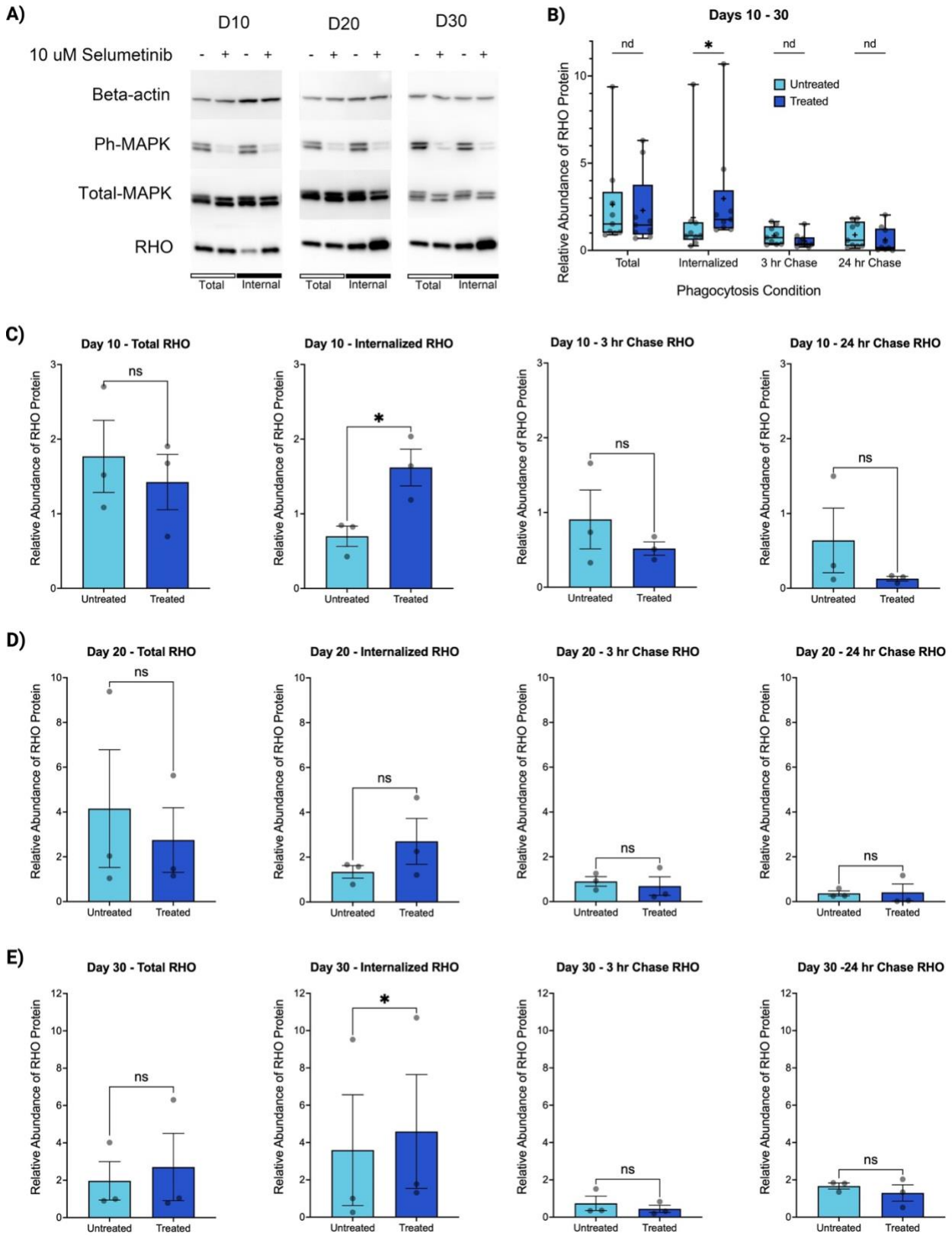
A)
D10
D20
D30
10 uM Selumetinib
Beta-actin
Ph-MAPK
Total-MAPK
RHO
Total
Internal
B)
Days 10 - 30
nd
*
Untreated
Treated
Relative Abundance of RHO Protein
Total
Internalized
3 hr Chase
24 hr Chase
Phagocytosis Condition
C)
Day 10 - Total RHO
Day 10 - Internalized RHO
Day 10 - 3 hr Chase RHO
Day 10 - 24 hr Chase RHO
ns
D)
Day 20 - Total RHO
Day 20 - Internalized RHO
Day 20 - 3 hr Chase RHO
Day 20 - 24 hr Chase RHO
E)
Day 30 - Total RHO
Day 30 - Internalized RHO
Day 30 - 3 hr Chase RHO
Day 30 -24 hr Chase RHO

813 **Figure 2 - Selumetinib treatment increases bROS internalization by hiPSC-derived**
814 **RPE cells. A)** Representative Western Blot of Total and Internalized phagocytosis
815 conditions show an increase in internalized RHO in hiPSC-derived RPE treated with 10
816 μM selumetinib versus untreated controls. **B)** When all treatment times were combined,
817 10 μM selumetinib significantly increases the internalization of RHO. There was no
818 significant difference between treatment conditions for other phagocytosis conditions
819 measured. Multiple paired t tests, Mean ± SEM, n = 9 pairs per phagocytosis condition.
820 **C)** At Day 10, 10 μM selumetinib significantly increases the internalization of RHO and
821 does not affect other phagocytosis conditions. **D)** At Day 20, there is no significant
822 difference in relative abundance of RHO between treatment groups given phagocytosis
823 conditions. **E)** At Day 30, 10 uM selumetinib significantly increases the internalization of
824 RHO and does not affect other phagocytosis conditions. **C-E)** Results of paired t tests,
825 Mean ± SEM, n = 3 pairs for each phagocytosis condition from independent
826 experiments. *, $p<0.05$. Abbreviations: D10, 10 days of selumetinib treatment; D20, 20
827 days of selumetinib treatment; D30, 30 days of selumetinib treatmenr; nd, no discovery;
828 ns, not significant.

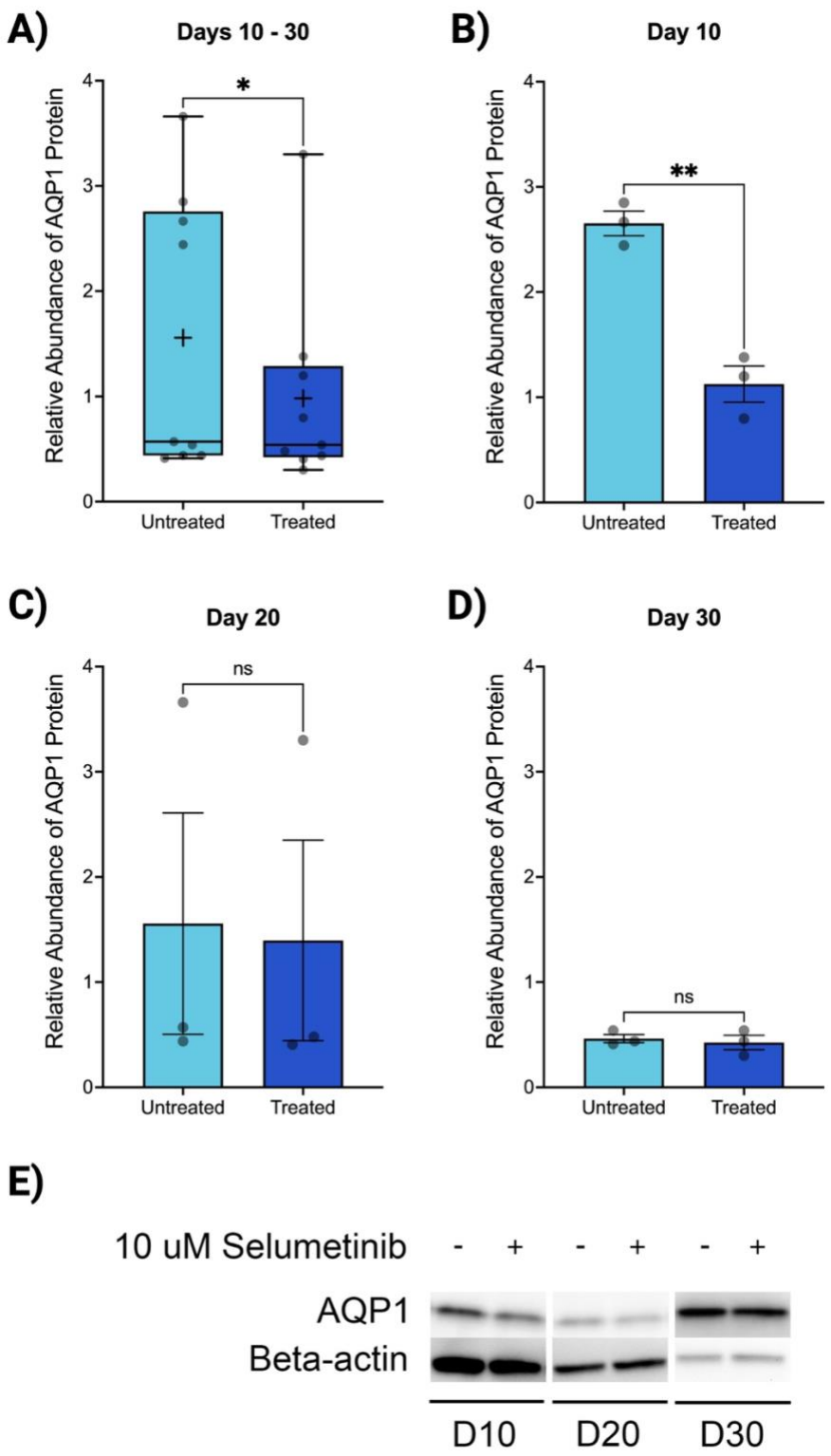


**Figure 3 - Selumetinib decreases aquaporin 1 (AQP1) expression. A)** AQP1 expression in hiPSC-derived RPE cells in combined 10- (B), 20- (C) and 30-day

832 selumetinib treatment groups versus untreated controls. For this analysis all treatment
833 times were combined. **B-D)** AQP1 expression in hiPSC-derived RPE cells following 10-
834 (B), 20- (C) and 30-days of selumetinib treatment versus untreated controls. Bars
835 represent Mean ± SEM, n = 3 pairs from independent experiments for each time point.
836 *, $p<0.05$; **, $p<0.002$. **E)** Representative Western blots depicting decreased AQP1
837 protein levels in hiPSC-derived RPE cells in selumetinib treated versus untreated
838 controls following 10-, 20-, and 30-days of treatment. AQP1 was significantly decreased
839 following 10 days of selumetinib treatment. The levels of AQP1 rebounded to normal by
840 20- and 30-days of selumetinib treatment.
841
842
843
844

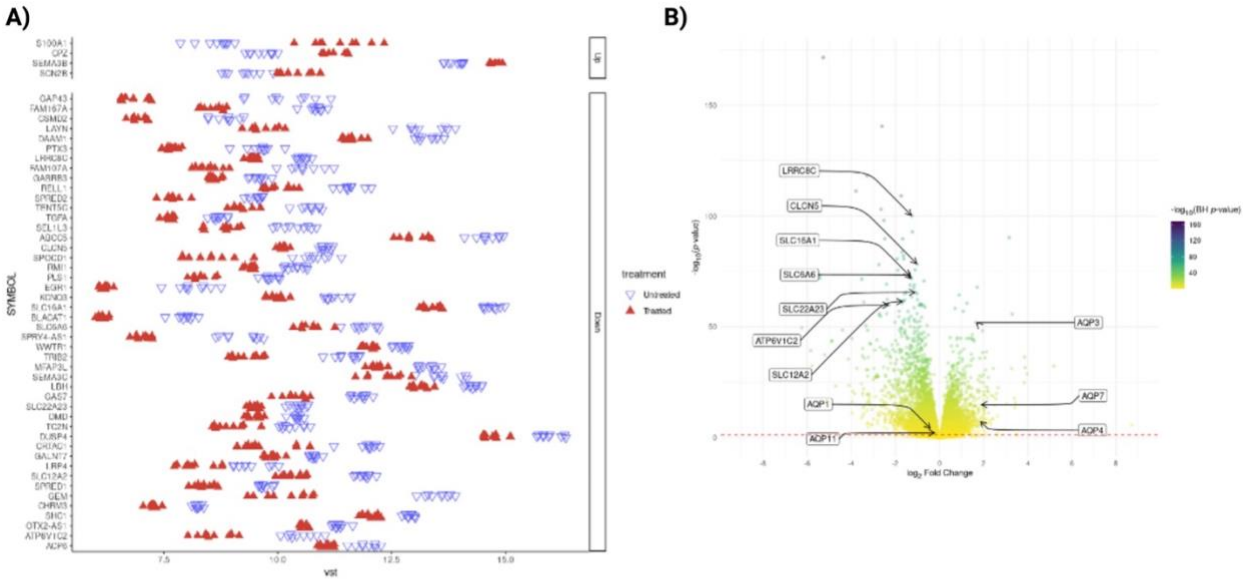


C)

| Top Altered Pathways | Bonferroni p-value |
|---|---|
| Neuroactive ligand-receptor interaction | $7.976 \times 10^{-9}$ |
| Calcium signaling | $9.719 \times 10^{-9}$ |
| PI3K-Akt signaling | $8.548 \times 10^{-6}$ |
| Extracellular matrix-receptor interaction | $1.604 \times 10^{-4}$ |

D)

| Top Altered Biological Processes (GO Term) | High-Specificity Pruning p-value |
|---|---|
| Visual perception | $6.511 \times 10^{-4}$ |
| Transport across blood-brain barrier | 0.002 |
| Positive regulation of cytosolic calcium ion concentration | 0.002 |
| Positive regulation of peptidyl-tyrosine phosphorylation | 0.002 |
| Positive regulation of ERK1 and ERK2 cascade | 0.002 |

**Figure 4 – Selumetinib significantly alters gene expression in hiPSC-derived RPE cells. A)** Beeswarm plot of top 50 DEGs. Y-axis ordering is determined by Benjamini-Hochberg (BH) adjusted p-value, with the lowest p-value at the top. **B)** Volcano plot of DEGs. Negative $\log_{10}$ of BH adjusted p-values. Estimates of fold change and significance were calculated from a pairwise contrast of treatment groups. Dashed red line indicates a p-value threshold of 0.05. **C)** Summary of top pathways altered genes between treatment groups using iPathwayGuide scores. **D)** Summary of top biological processes altered between treatment groups using Gene Ontology (GO) Analysis. Abbreviations: VST, variance stabilizing transformation; DEG, differentially expressed genes; GO, gene ontology; D10, 10 days of selumetinib treatment; D20, 20 days of selumetinib treatment; D30, 30 days of selumetinib treatment.

880 **REFERENCES**


881 1. Ram T, Singh AK, Kumar A, Singh H, Pathak P, Grishina M, et al. MEK inhibitors in
882 cancer treatment: structural insights, regulation, recent advances and future
883 perspectives. *RSC Med Chem*. 2023;14(10):1837-57.
884 2. Merrill NM, Vandecan NM, Day KC, Palmbos PL, Day ML, Udager AM, et al. MEK is a
885 promising target in the basal subtype of bladder cancer. *Oncotarget*.
886 2020;11(44):3921-32.
887 3. Nickols NG, Nazarian R, Zhao SG, Tan V, Uzunangelov V, Xia Z, et al. MEK-ERK
888 signaling is a therapeutic target in metastatic castration resistant prostate cancer.
889 *Prostate Cancer Prostatic Dis*. 2019;22(4):531-8.
890 4. Weber ML, Liang MC, Flaherty KT, and Heier JS. Subretinal Fluid Associated With
891 MEK Inhibitor Use in the Treatment of Systemic Cancer. *JAMA Ophthalmol*.
892 2016;134(8):855-62.
893 5. Francis JH, Habib LA, Abramson DH, Yannuzzi LA, Heinemann M, Gounder MM, et
894 al. Clinical and Morphologic Characteristics of MEK Inhibitor-Associated
895 Retinopathy: Differences from Central Serous Chorioretinopathy. *Ophthalmology*.
896 2017;124(12):1788-98.
897 6. Francis JH, Harding JJ, Schram AM, Canestraro J, Haggag-Lindgren D, Heinemann
898 M, et al. Clinical and Morphologic Characteristics of Fibroblast Growth Factor
899 Receptor Inhibitor-Associated Retinopathy. *JAMA Ophthalmol*. 2021;139(10):1126-
900 30.

901 7. Francis JH, Canestraro J, Haggag-Lindgren D, Harding JJ, Diamond EL, Drilon A, et
902 al. Clinical and Morphologic Characteristics of Extracellular Signal-Regulated
903 Kinase Inhibitor-Associated Retinopathy. *Ophthalmol Retina*. 2021;5(12):1187-95.
904 8. Urner-Bloch U, Urner M, Stieger P, Galliker N, Winterton N, Zubel A, et al. Transient
905 MEK inhibitor-associated retinopathy in metastatic melanoma. *Annals of Oncology*.
906 2014;25(7):1437-41.
907 9. McCannel TA, Chmielowski B, Finn RS, Goldman J, Ribas A, Wainberg ZA, et al.
908 Bilateral Subfoveal Neurosensory Retinal Detachment Associated With MEK
909 Inhibitor Use for Metastatic Cancer. *JAMA Ophthalmology*. 2014;132(8):1005-9.
910 10. Jeng-Miller KW, Miller MA, and Heier JS. Ocular Effects of MEK Inhibitor Therapy:
911 Literature Review, Clinical Presentation, and Best Practices for Mitigation.
912 *Oncologist*. 2024;29(5):e616-e21.
913 11. Yang S, Zhou J, and Li D. Functions and Diseases of the Retinal Pigment Epithelium.
914 *Front Pharmacol*. 2021;12:727870.
915 12. Lehmann GL, Benedicto I, Philp NJ, and Rodriguez-Boulan E. Plasma membrane
916 protein polarity and trafficking in RPE cells: past, present and future. *Exp Eye Res*.
917 2014;126:5-15.
918 13. Lakkaraju A, Umapathy A, Tan LX, Daniele L, Philp NJ, Boesze-Battaglia K, et al. The
919 cell biology of the retinal pigment epithelium. *Progress in Retinal and Eye Research*.
920 2020;78:100846.

921 14. Wiley LA, Burnight ER, DeLuca AP, Anfinson KR, Cranston CM, Kaalberg EE, et al.
922 cGMP production of patient-specific iPSCs and photoreceptor precursor cells to
923 treat retinal degenerative blindness. *Scientific Reports*. 2016;6(1):30742.
924 15. Foltz LP, and Clegg DO. Rapid, Directed Differentiation of Retinal Pigment Epithelial
925 Cells from Human Embryonic or Induced Pluripotent Stem Cells. *J Vis Exp*.
926 2017(128).
927 16. Nolan ND, Jenny LA, Wang NK, and Tsang SH. Retinal pigment epithelium lipid
928 metabolic demands and therapeutic restoration. *Taiwan J Ophthalmol*.
929 2021;11(3):216-20.
930 17. Schreiter S, Vafia K, Barsacchi R, Tsang SH, Bickle M, Ader M, et al. A Human Retinal
931 Pigment Epithelium-Based Screening Platform Reveals Inducers of Photoreceptor
932 Outer Segments Phagocytosis. *Stem Cell Reports*. 2020;15(6):1347-61.
933 18. Stamer WD, Bok D, Hu J, Jaffe GJ, and McKay BS. Aquaporin-1 Channels in Human
934 Retinal Pigment Epithelium: Role in Transepithelial Water Movement. *Investigative*
935 *Ophthalmology & Visual Science*. 2003;44(6):2803-8.
936 19. Juuti-Uusitalo K, Delporte C, Grégoire F, Perret J, Huhtala H, Savolainen V, et al.
937 Aquaporin Expression and Function in Human Pluripotent Stem Cell–Derived
938 Retinal Pigmented Epithelial Cells. *Investigative Ophthalmology & Visual Science*.
939 2013;54(5):3510-9.
940 20. Jiang Q, Cao C, Lu S, Kivlin R, Wallin B, Chu W, et al. MEK/ERK pathway mediates
941 UVB-induced AQP1 downregulation and water permeability impairment in human
942 retinal pigment epithelial cells. *Int J Mol Med*. 2009;23(6):771-7.

943 21. Brutsaert EF. Diabetic Ketoacidosis (DKA).
944 https://www.msdmanuals.com/professional/endocrine-and-metabolic-
945 disorders/diabetes-mellitus-and-disorders-of-carbohydrate-metabolism/diabetic-
946 ketoacidosis-dka. Updated 2023/10, 2023.
947 22. Isales CM, Min L, and Hoffman WH. Acetoacetate and beta-hydroxybutyrate
948 differentially regulate endothelin-1 and vascular endothelial growth factor in mouse
949 brain microvascular endothelial cells. *J Diabetes Complications*. 1999;13(2):91-7.
950 23. Aiello LP, Bursell SE, Clermont A, Duh E, Ishii H, Takagi C, et al. Vascular endothelial
951 growth factor-induced retinal permeability is mediated by protein kinase C in vivo
952 and suppressed by an orally effective beta-isoform-selective inhibitor. *Diabetes*.
953 1997;46(9):1473-80.
954 24. Cheng Y, and Tian H. Current Development Status of MEK Inhibitors. *Molecules*.
955 2017;22(10):1551.
956 25. Baetz NW, Stamer WD, and Yool AJ. Stimulation of aquaporin-mediated fluid
957 transport by cyclic GMP in human retinal pigment epithelium in vitro. *Invest*
958 *Ophthalmol Vis Sci*. 2012;53(4):2127-32.
959 26. Liew G, Ho IV, Ong S, Gopinath B, and Mitchell P. Efficacy of Topical Carbonic
960 Anhydrase Inhibitors in Reducing Duration of Chronic Central Serous
961 Chorioretinopathy. *Transl Vis Sci Technol*. 2020;9(13):6.
962 27. Wolfensberger TJ, Mahieu I, Jarvis-Evans J, Boulton M, Carter ND, Nógrádi A, et al.
963 Membrane-bound carbonic anhydrase in human retinal pigment epithelium. *Invest*
964 *Ophthalmol Vis Sci*. 1994;35(9):3401-7.

965 28. Wolfensberger TJ. The role of carbonic anhydrase inhibitors in the management of
966 macular edema. *Doc Ophthalmol*. 1999;97(3-4):387-97.
967 29. Cox SN, Hay E, and Bird AC. Treatment of chronic macular edema with
968 acetazolamide. *Arch Ophthalmol*. 1988;106(9):1190-5.
969 30. Zhang L, Reyes R, Lee W, Chen CL, Chan L, Sujirakul T, et al. Rapid resolution of
970 retinoschisis with acetazolamide. *Doc Ophthalmol*. 2015;131(1):63-70.
971 31. Grover S, Fishman GA, Fiscella RG, and Adelman AE. Efficacy of dorzolamide
972 hydrochloride in the management of chronic cystoid macular edema in patients
973 with retinitis pigmentosa. *Retina*. 1997;17(3):222-31.
974 32. Wuarin R, Kakkassery V, Consigli A, Roquelaure D, Papanastasiou A, Schutz JS, et
975 al. Combined Topical Anti-inflammatory and Oral Acetazolamide in the Treatment
976 of Central Serous Chorioretinopathy. *Optom Vis Sci*. 2019;96(7):500-6.
977 33. Pikkel J, Beiran I, Ophir A, and Miller B. Acetazolamide for central serous
978 retinopathy. *Ophthalmology*. 2002;109(9):1723-5.
979 34. Wolfensberger TJ, Chiang RK, Takeuchi A, and Marmor MF. Inhibition of membrane-
980 bound carbonic anhydrase enhances subretinal fluid absorption and retinal
981 adhesiveness. *Graefes Arch Clin Exp Ophthalmol*. 2000;238(1):76-80.
982 35. Shahsuvaryan ML. Carbonic anhydrase inhibitors in the management of macular
983 edema: A review of the literature. *Med Hypothesis Discov Innov Ophthalmol*.
984 2022;11(1):34-41.
985 36. Orgül S, Reuter U, and Kain HL. Osmotic stress in an in vitro model of the outer
986 blood-retinal barrier. *Ger J Ophthalmol*. 1993;2(6):436-43.

987 37. Ghouli MR, Fiacco TA, and Binder DK. Structure-function relationships of the LRRC8
988 subunits and subdomains of the volume-regulated anion channel (VRAC). *Front*
989 *Cell Neurosci*. 2022;16:962714.
990 38. Li P, Hu M, Wang C, Feng X, Zhao Z, Yang Y, et al. LRRC8 family proteins within
991 lysosomes regulate cellular osmoregulation and enhance cell survival to multiple
992 physiological stresses. *Proc Natl Acad Sci U S A*. 2020;117(46):29155-65.
993 39. Gianesello L, Del Prete D, Ceol M, Priante G, Calò LA, and Anglani F. From protein
994 uptake to Dent disease: An overview of the CLCN5 gene. *Gene*. 2020;747:144662.
995 40. Adijanto J, and Philp NJ. The SLC16A family of monocarboxylate transporters
996 (MCTs)--physiology and function in cellular metabolism, pH homeostasis, and fluid
997 transport. *Curr Top Membr*. 2012;70:275-311.
998 41. Philp NJ, Yoon H, and Grollman EF. Monocarboxylate transporter MCT1 is located in
999 the apical membrane and MCT3 in the basal membrane of rat RPE. *Am J Physiol*.
1000 1998;274(6):R1824-8.
1001 42. Milićević N, Ten Brink JB, Ten Asbroek A, Bergen AA, and Felder-Schmittbuhl MP.
1002 The circadian clock regulates RPE-mediated lactate transport via SLC16A1 (MCT1).
1003 *Exp Eye Res*. 2020;190:107861.
1004 43. . SLC6A6 solute carrier family 6 member 6 [ Homo sapiens (human) ].
1005 https://www.ncbi.nlm.nih.gov/gene/6533. Accessed September 22, 2025.
1006 44. Huxtable RJ. Physiological actions of taurine. *Physiol Rev*. 1992;72(1):101-63.

1007 45. Preising MN, Görg B, Friedburg C, Qvartskhava N, Budde BS, Bonus M, et al.
1008 Biallelic mutation of human SLC6A6 encoding the taurine transporter TAUT is linked
1009 to early retinal degeneration. *The FASEB Journal*. 2019;33(10):11507-27.
1010 46. El-Sherbeny A, Naggar H, Miyauchi S, Ola MS, Maddox DM, Martin PM, et al.
1011 Osmoregulation of taurine transporter function and expression in retinal pigment
1012 epithelial, ganglion, and müller cells. *Invest Ophthalmol Vis Sci*. 2004;45(2):694-
1013 701.
1014 47. Heller-Stilb B, van Roeyen C, Rascher K, Hartwig HG, Huth A, Seeliger MW, et al.
1015 Disruption of the taurine transporter gene (taut) leads to retinal degeneration in
1016 mice. *Faseb j*. 2002;16(2):231-3.
1017 48. Hellinen L, Sato K, Reinisalo M, Kidron H, Rilla K, Tachikawa M, et al. Quantitative
1018 Protein Expression in the Human Retinal Pigment Epithelium: Comparison Between
1019 Apical and Basolateral Plasma Membranes With Emphasis on Transporters.
1020 *Investigative Ophthalmology & Visual Science*. 2019;60(15):5022-34.
1021 49. Nigam SK. The SLC22 Transporter Family: A Paradigm for the Impact of Drug
1022 Transporters on Metabolic Pathways, Signaling, and Disease. *Annu Rev Pharmacol*
1023 *Toxicol*. 2018;58:663-87.
1024 50. Koumangoye R, Bastarache L, and Delpire E. NKCC1: Newly Found as a Human
1025 Disease-Causing Ion Transporter. *Function (Oxf)*. 2021;2(1):zqaa028.
1026 51. Russell JM. Sodium-potassium-chloride cotransport. *Physiol Rev*. 2000;80(1):211-
1027 76.

1028 52. Hengl T, Kaneko H, Dauner K, Vocke K, Frings S, and Möhrlen F. Molecular
1029 components of signal amplification in olfactory sensory cilia. *Proc Natl Acad Sci U S*
1030 *A*. 2010;107(13):6052-7.
1031 53. Milićević N, Duursma A, Ten Asbroek A, Felder-Schmittbuhl MP, and Bergen AA.
1032 Does the circadian clock make RPE-mediated ion transport "tick" via SLC12A2
1033 (NKCC1)? *Chronobiol Int*. 2019;36(11):1592-8.
1034 54. Plotkin MD, Kaplan MR, Peterson LN, Gullans SR, Hebert SC, and Delpire E.
1035 Expression of the Na(+)-K(+)-2Cl- cotransporter BSC2 in the nervous system. *Am J*
1036 *Physiol*. 1997;272(1 Pt 1):C173-83.
1037 55. Wu Q, Delpire E, Hebert SC, and Strange K. Functional demonstration of Na+-K+-
1038 2Cl- cotransporter activity in isolated, polarized choroid plexus cells. *Am J Physiol*.
1039 1998;275(6):C1565-72.
1040 56. . ATP6V1C2 ATPase H+ transporting V1 subunit C2 [ Homo sapiens (human) ].
1041 https://www.ncbi.nlm.nih.gov/gene/245973. Accessed September 22, 2025.
1042 57. Santos-Pereira C, Rodrigues LR, and Côrte-Real M. Emerging insights on the role of
1043 V-ATPase in human diseases: Therapeutic challenges and opportunities. *Med Res*
1044 *Rev*. 2021;41(4):1927-64.
1045 58. Jobst-Schwan T, Klämbt V, Tarsio M, Heneghan JF, Majmundar AJ, Shril S, et al.
1046 Whole exome sequencing identified ATP6V1C2 as a novel candidate gene for
1047 recessive distal renal tubular acidosis. *Kidney Int*. 2020;97(3):567-79.

1048 59. Futai M, Sun-Wada GH, Wada Y, Matsumoto N, and Nakanishi-Matsui M. Vacuolar-
1049 type ATPase: A proton pump to lysosomal trafficking. *Proc Jpn Acad Ser B Phys Biol*
1050 *Sci.* 2019;95(6):261-77.
1051 60. Voigt AP, Whitmore SS, Mulfaul K, Chirco KR, Giacalone JC, Flamme-Wiese MJ, et
1052 al. Bulk and single-cell gene expression analyses reveal aging human
1053 choriocapillaris has pro-inflammatory phenotype. *Microvasc Res.*
1054 2020;131:104031.
1055 61. Voigt AP, Whitmore SS, Lessing ND, DeLuca AP, Tucker BA, Stone EM, et al.
1056 Spectacle: An interactive resource for ocular single-cell RNA sequencing data
1057 analysis. *Experimental Eye Research.* 2020;200:108204.
1058 62. Voigt AP, Whitmore SS, Flamme-Wiese MJ, Riker MJ, Wiley LA, Tucker BA, et al.
1059 Molecular characterization of foveal versus peripheral human retina by single-cell
1060 RNA sequencing. *Exp Eye Res.* 2019;184:234-42.
1061 63. Voigt AP, Mulfaul K, Mullin NK, Flamme-Wiese MJ, Giacalone JC, Stone EM, et al.
1062 Single-cell transcriptomics of the human retinal pigment epithelium and choroid in
1063 health and macular degeneration. *Proc Natl Acad Sci U S A.* 2019;116(48):24100-7.
1064 64. Voigt AP, Binkley E, Flamme-Wiese MJ, Zeng S, DeLuca AP, Scheetz TE, et al. Single-
1065 Cell RNA Sequencing in Human Retinal Degeneration Reveals Distinct Glial Cell
1066 Populations. *Cells.* 2020;9(2).
1067 65. Shine L, Kilty C, Gross J, and Kennedy B. Vacuolar ATPases and their role in vision.
1068 *Adv Exp Med Biol.* 2014;801:97-103.

1069 66. Deguchi J, Yamamoto A, Yoshimori T, Sugasawa K, Moriyama Y, Futai M, et al.
1070 Acidification of phagosomes and degradation of rod outer segments in rat retinal
1071 pigment epithelium. *Invest Ophthalmol Vis Sci.* 1994;35(2):568-79.
1072 67. Bergmann M, Schütt F, Holz FG, and Kopitz J. Inhibition of the ATP-driven proton
1073 pump in RPE lysosomes by the major lipofuscin fluorophore A2-E may contribute to
1074 the pathogenesis of age-related macular degeneration. *Faseb j.* 2004;18(3):562-4.
1075 68. de Nadal E, Alepuz PM, and Posas F. Dealing with osmostress through MAP kinase
1076 activation. *EMBO Rep.* 2002;3(8):735-40.
1077 69. Hollborn M, Ulbricht E, Reichenbach A, Wiedemann P, Bringmann A, and Kohen L.
1078 Transcriptional regulation of aquaporin-3 in human retinal pigment epithelial cells.
1079 *Mol Biol Rep.* 2012;39(8):7949-56.
1080 70. Willermain F, Janssens S, Arsenijevic T, Piens I, Bolaky N, Caspers L, et al. Osmotic
1081 stress decreases aquaporin-4 expression in the human retinal pigment epithelial
1082 cell line, ARPE-19. *Int J Mol Med.* 2014;34(2):533-8.
1083 71. Frühbeck G, Catalán V, Gómez-Ambrosi J, and Rodríguez A. Aquaporin-7 and
1084 glycerol permeability as novel obesity drug-target pathways. *Trends Pharmacol Sci.*
1085 2006;27(7):345-7.
1086 72. Kondo H, Shimomura I, Kishida K, Kuriyama H, Makino Y, Nishizawa H, et al. Human
1087 aquaporin adipose (AQPap) gene. Genomic structure, promoter analysis and
1088 functional mutation. *Eur J Biochem.* 2002;269(7):1814-26.

1089 73. Zhang C, Luo D, Xie H, Yang Q, Liu D, Tang L, et al. Aquaporin 11 alleviates retinal
1090 Müller intracellular edema through water efflux in diabetic retinopathy.
1091 *Pharmacological Research*. 2023;187:106559.
1092 74. Boon CJF, Klevering BJ, Leroy BP, Hoyng CB, Keunen JEE, and den Hollander AI. The
1093 spectrum of ocular phenotypes caused by mutations in the BEST1 gene. *Progress in*
1094 *Retinal and Eye Research*. 2009;28(3):187-205.
1095 75. Fischmeister R, and Hartzell HC. Volume sensitivity of the bestrophin family of
1096 chloride channels. *J Physiol*. 2005;562(Pt 2):477-91.
1097 76. Petrukhin K, Koisti MJ, Bakall B, Li W, Xie G, Marknell T, et al. Identification of the
1098 gene responsible for Best macular dystrophy. *Nat Genet*. 1998;19(3):241-7.
1099 77. Marquardt A, Stöhr H, Passmore LA, Krämer F, Rivera A, and Weber BH. Mutations
1100 in a novel gene, VMD2, encoding a protein of unknown properties cause juvenile-
1101 onset vitelliform macular dystrophy (Best's disease). *Hum Mol Genet*.
1102 1998;7(9):1517-25.
1103 78. Marmorstein AD, Marmorstein LY, Rayborn M, Wang X, Hollyfield JG, and Petrukhin
1104 K. Bestrophin, the product of the Best vitelliform macular dystrophy gene (VMD2),
1105 localizes to the basolateral plasma membrane of the retinal pigment epithelium.
1106 *Proc Natl Acad Sci U S A*. 2000;97(23):12758-63.
1107 79. Mullins RF, Kuehn MH, Faidley EA, Syed NA, and Stone EM. Differential macular and
1108 peripheral expression of bestrophin in human eyes and its implication for best
1109 disease. *Invest Ophthalmol Vis Sci*. 2007;48(7):3372-80.

1110 80. Jentsch TJ. Chloride and the endosomal-lysosomal pathway: emerging roles of CLC
1111 chloride transporters. *J Physiol*. 2007;578(Pt 3):633-40.
1112 81. Karl MO, Kroeger W, Wimmers S, Milenkovic VM, Valtink M, Engelmann K, et al.
1113 Endogenous Gas6 and Ca2+ -channel activation modulate phagocytosis by retinal
1114 pigment epithelium. *Cell Signal*. 2008;20(6):1159-68.
1115 82. Singh R, Shen W, Kuai D, Martin JM, Guo X, Smith MA, et al. iPS cell modeling of Best
1116 disease: insights into the pathophysiology of an inherited macular degeneration.
1117 *Hum Mol Genet*. 2013;22(3):593-607.
1118 83. Gulette GA, Hass DT, Pandey K, Zhang Q, Han JYS, Engel A, et al. Reassessing
1119 retinal pigment epithelial ketogenesis: Enzymatic assays for ketone body levels
1120 provide inaccurate results. *Exp Eye Res*. 2024;245:109966.
1121 84. Adijanto J, Du J, Moffat C, Seifert EL, Hurle JB, and Philp NJ. The retinal pigment
1122 epithelium utilizes fatty acids for ketogenesis. *J Biol Chem*. 2014;289(30):20570-82.
1123 85. Du SW, and Palczewski K. MicroRNA regulation of critical retinal pigment epithelial
1124 functions. *Trends Neurosci*. 2022;45(1):78-90.
1125 86. Jiang C, Xie P, Sun R, Sun X, Liu G, Ding S, et al. c-Jun-mediated microRNA-302d-3p
1126 induces RPE dedifferentiation by targeting p21(Waf1/Cip1). *Cell Death Dis*.
1127 2018;9(5):451.
1128 87. Croze RH, Buchholz DE, Radeke MJ, Thi WJ, Hu Q, Coffey PJ, et al. ROCK Inhibition
1129 Extends Passage of Pluripotent Stem Cell-Derived Retinal Pigmented Epithelium.
1130 *Stem Cells Translational Medicine*. 2014;3(9):1066-78.

1131 88. Ewels PA, Peltzer A, Fillinger S, Patel H, Alneberg J, Wilm A, et al. The nf-core
1132 framework for community-curated bioinformatics pipelines. *Nature Biotechnology*.
1133 2020;38(3):276-8.
1134 89. Grüning B, Dale R, Sjödin A, Chapman BA, Rowe J, Tomkins-Tinch CH, et al.
1135 Bioconda: sustainable and comprehensive software distribution for the life
1136 sciences. *Nature Methods*. 2018;15(7):475-6.
1137 90. da Veiga Leprevost F, Grüning BA, Alves Aflitos S, Röst HL, Uszkoreit J, Barsnes H, et
1138 al. BioContainers: an open-source and community-driven framework for software
1139 standardization. *Bioinformatics*. 2017;33(16):2580-2.
1140 91. Di Tommaso P, Chatzou M, Floden EW, Barja PP, Palumbo E, and Notredame C.
1141 Nextflow enables reproducible computational workflows. *Nature Biotechnology*.
1142 2017;35(4):316-9.
1143 92. Krueger F. 2023.
1144 93. Martin M. Cutadapt removes adapter sequences from high-throughput sequencing
1145 reads. *EMBnetjournal*. 2011;17(1):10-2.
1146 94. Cock PJA, Fields CJ, Goto N, Heuer ML, and Rice PM. The Sanger FASTQ file format
1147 for sequences with quality scores, and the Solexa/Illumina FASTQ variants. *Nucleic*
1148 *Acids Research*. 2010;38(6):1767-71.
1149 95. Andrews S. 2023.
1150 96. Patro R, Duggal G, Love MI, Irizarry RA, and Kingsford C. Salmon provides fast and
1151 bias-aware quantification of transcript expression. *Nature Methods*.
1152 2017;14(4):417-9.

1153 97. Srivastava A, Malik L, Sarkar H, Zakeri M, Almodaresi F, Soneson C, et al. Alignment
1154 and mapping methodology influence transcript abundance estimation. *Genome*
1155 *Biology*. 2020;21(1):239.
1156 98. Team RC. Vienna, Austria: R Foundation for Statistical Computing; 2024.
1157 99. Huber W, Carey VJ, Gentleman R, Anders S, Carlson M, Carvalho BS, et al.
1158 Orchestrating high-throughput genomic analysis with Bioconductor. *Nature*
1159 *Methods*. 2015;12(2):115-21.
1160 100. Soneson C, Love MI, and Robinson MD. Differential analyses for RNA-seq:
1161 transcript-level estimates improve gene-level inferences [version 2; peer review: 2
1162 approved]. *F1000Research*. 2016;4(1521).
1163 101. Love MI, Soneson C, Hickey PF, Johnson LK, Pierce NT, Shepherd L, et al. Tximeta:
1164 Reference sequence checksums for provenance identification in RNA-seq. *PLOS*
1165 *Computational Biology*. 2020;16(2):e1007664.
1166 102. Pagès H, Carlson M, Falcon S, and Li N. 2024.
1167 103. Carlson M. 2024.
1168 104. Morgan M, Obenchain V, Hester J, and Pagès H. 2024.
1169 105. Mangiola S, Molania R, Dong R, Doyle MA, and Papenfuss AT. tidybulk: an R tidy
1170 framework for modular transcriptomic data analysis. *Genome Biology*.
1171 2021;22(1):42.
1172 106. Chen Y, Lun ATL, and Smyth GK. From reads to genes to pathways: differential
1173 expression analysis of RNA-Seq experiments using Rsubread and the edgeR quasi-

likelihood pipeline [version 2; peer review: 5 approved]. *F1000Research*. 2016;5(1438).

107. Love MI, Huber W, and Anders S. Moderated estimation of fold change and dispersion for RNA-seq data with DESeq2. *Genome Biology*. 2014;15(12):550.

108. Law CW, Zeglinski K, Dong X, Alhamdoosh M, Smyth GK, and Ritchie ME. A guide to creating design matrices for gene expression experiments [version 1; peer review: 2 approved]. *F1000Research*. 2020;9(1444).

109. Ahsan S, and Drăghici S. Identifying Significantly Impacted Pathways and Putative Mechanisms with iPathwayGuide. *Current Protocols in Bioinformatics*. 2017;57(1):7.15.1-7..30.